Highlights

Benchmarking multiphysics software for mantle convection

Sean J. Trim,Samuel L. Butler,Raymond J. Spiteri

- COMSOL® is tested using several mantle convection benchmarks
- COMSOL® can cope with extreme viscosity contrasts and non-Newtonian rheology
- Software settings appropriate to mantle convection are discussed

Benchmarking multiphysics software for mantle convection

Sean J. Trim[a,*,1], Samuel L. Butler[b,2] and Raymond J. Spiteri[a,3]

[a]Department of Computer Science, 176 Thorvaldson Bldg, 110 Science Place, University of Saskatchewan, Saskatoon, SK, S7N 5C9, Canada
[b]Department of Geological Sciences, Geology Bldg, 114 Science Place, University of Saskatchewan, Saskatoon, SK, S7N 5E2, Canada

ARTICLE INFO

Keywords:
COMSOL Multiphysics®
mantle convection
benchmark
finite elements

ABSTRACT

Due to the inaccessibility of the mantle to direct measurements, numerical simulations are a highly valuable tool for improving our understanding of its dynamics. COMSOL Multiphysics® is a commercial software suite designed to numerically model experiments featuring multiple branches of physics. This modeling approach applies to mantle convection, which can be viewed as a combination of fluid dynamics and thermodynamics. COMSOL® is of interest to the geoscience community due to its ease of use compared to other available codes and it has been used in previous mantle convection studies. However, COMSOL® has not been formally benchmarked for mantle convection. In this study, we confirm the accuracy of COMSOL® against several established benchmarks pertaining to a variety mantle convection features and geometries. Overall, we find good agreement between the results from COMSOL® and reported benchmark data. This study may also serve the geoscience community as a guide for using COMSOL® to model mantle convection.

1. Introduction

The mantle, comprising more than 80% of the Earth's total volume, is of primary importance in our planet's evolution. For instance, the mantle is the link between physical processes near the outer core and the dynamics occurring on the planet's surface. Despite being separated by nearly 3000 kilometers, the dynamics of the Core-Mantle Boundary (CMB) can significantly influence motion at the Earth's surface. For example, numerical simulations have shown that compositional variations near the CMB (e.g., Humayun et al., 2004; Ishii and Tromp, 2004; Labrosse et al., 2007) can impact the velocities of tectonic plates (Trim et al., 2014) and the frequency of supercontinent formation (Trim and Lowman, 2016). Plate motion can also affect compositional topography above the CMB (McNamara and Zhong, 2005). The process of mantle convection controls the rate at which heat is lost from the Earth's interior (Turcotte and Schubert, 2002). The Earth's ability to generate a magnetic field, the protector of our upper atmosphere, largely relies on sufficient heat flow from the core into the mantle (Buffett, 2002). The morphology of the geomagnetic field is also dependent on the structure of the deep mantle (Gubbins et al., 2007).

The mantle acts as a solid over everyday time scales. For example, the mantle is known to transmit seismic S waves. However, over geologic time scales, the mantle can be modeled as a highly viscous fluid (Turcotte and Schubert, 2002). Modeling mantle convection is difficult because of several factors, including strongly temperature-dependent viscosity,

*Corresponding author
sean.trim@usask.ca (S.J. Trim)
ORCID(s):
[1]Contributed to manuscript text. Performed all calculations and quantitative analysis.
[2]Originator of study concept. Contributed to manuscript text and scientific analysis. Also provided computational resources.
[3]Contributed to manuscript text. Provided expertise in numerical methods.

non-Newtonian processes, sharp compositional variations and spherical curvature. COMSOL Multiphysics® is a commercial software package capable of simulating a wide range of situations, due to its ability to freely combine a variety of different physics modules. Another advantage of the software is the relative ease of use compared to other production codes. In particular, the user is not required to have experience in numerics or programming (although knowledge of numerical methods is an asset when adjusting some options). Accordingly, COMSOL® is also a viable option for introducing students to geodynamic modeling. COMSOL® has been utilized in the geosciences (Azad et al., 2016; Bird et al., 2014; Butler and Sinha, 2012; Butler and Zhang, 2016; Halloran et al., 2019; Li and Smith, 2015; Nardi et al., 2014; Pirnia et al., 2019), including mantle convection studies (Herein and Galsa, 2011; Lee, 2014; Lee and Wada, 2017; Shahraki and Schmeling, 2012; Sinha and Butler, 2009; Shiels and Butler, 2015). However, it appears the software has not been benchmarked in detail for mantle convection problems. This study provides a detailed performance analysis of COMSOL® on six benchmark mantle convection problems and also describes a framework for utilizing COMSOL® to model mantle convection.

We have selected six benchmark studies to test COMSOL® over a range of different mantle convection features. The problems are summarized as follows (further details are given in section 4):

(1) Blankenbach et al. (1989): 2D Cartesian flow with a) constant viscosity and b) moderately strong temperature-dependent viscosity.

(2) Busse et al. (1994): 3D Cartesian flow with both a) constant and b) temperature-dependent viscosity.

(3) Moresi and Solomatov (1995): 2D Cartesian flow with extremely temperature-dependent viscosity.

(4) Tosi et al. (2015): 2D Cartesian flow with non-Newtonian surface rheology and temperature-dependent viscosity featuring a) stagnant-lid and b) mobile-lid convective regimes.

(5) van Keken et al. (1997): Isoviscous Rayleigh–Taylor instability driven by compositional buoyancy contrasts in 2D Cartesian geometry.

(6) Zhong et al. (2008): 3D spherical convection with a) constant and b)–e) temperature-dependent viscosities.

For reference, the geometry, buoyancy type, and viscosity type for each problem are summarized in Table 1.

2. Governing Equations

Mathematically, the fluid mantle is described by conservation equations for mass, momentum, energy, and composition. Although these equations may be written in dimensional form (e.g., in SI units), they are usually recast in dimensionless form. This allows identification of key nondimensional controlling parameters (such as the thermal Rayleigh number) and simplifies scaling of terms. The Boussinesq approximation is used to simplify how compressibility is modeled. Specifically, compressibility effects are presumed negligible, except as they impact buoyancy. The infinite

Table 1
Summary of geometry, buoyancy type, and viscosity type for each benchmark problem. For the viscosity type, T and $\dot{\epsilon}$ correspond to temperature and strain-rate, respectively.

Problem	Geometry	Buoyancy	Viscosity
1a	2D Cartesian	Thermal	Isoviscous
1b	2D Cartesian	Thermal	T-dependent
2a	3D Cartesian	Thermal	Isoviscous
2b	3D Cartesian	Thermal	T-dependent
3	2D Cartesian	Thermal	extreme T dependence
4a	2D Cartesian	Thermal	strong T dependence
4b	2D Cartesian	Thermal	strong T and $\dot{\epsilon}$ dependence
5	2D Cartesian	Compositional	Isoviscous
6a	3D Spherical	Thermal	Isoviscous
6b–e	3D Spherical	Thermal	T-dependent

Prandtl number approximation is also employed. Accordingly, inertial terms (including time derivative, advection, and Coriolis terms) in the Navier–Stokes equations, governing momentum conservation, vanish. The nondimensional conservation equations for mass, momentum, energy, and composition are:

$$\nabla \cdot \mathbf{v} = 0, \tag{1}$$

$$\nabla \cdot \left(2\eta \underline{\underline{\dot{\epsilon}}}\right) - \nabla P = \gamma \left(Ra_T T - Ra_C C\right) \hat{\mathbf{g}}, \tag{2}$$

$$\frac{\partial T}{\partial t} + \mathbf{v} \cdot \nabla T = \nabla^2 T \tag{3}$$

and

$$\frac{\partial C}{\partial t} + \mathbf{v} \cdot \nabla C = 0, \tag{4}$$

where $\mathbf{v}$ is the velocity; η is the viscosity; $\underline{\underline{\dot{\epsilon}}}$ is the strain rate tensor; P is the pressure; T is the temperature; C is the composition; $\hat{\mathbf{g}}$ is a unit vector in the direction of gravity; and t is time. The factor of γ rescales the buoyancy terms in the case of spherical geometry. In those cases, the scale factor is required because we choose a radial coordinate of zero to represent the center of the sphere. For Cartesian cases, $\gamma = 1$. For spherical cases, $\gamma = (R/D)^3$, where $R = 6370$ km is the Earth's radius and $D = 2900$ km is the thickness of the mantle.

The thermal and compositional Rayleigh numbers are defined as

$$Ra_T = \frac{\alpha \rho_0 g \Delta T D^3}{\kappa \eta_0} \tag{5}$$

and

$$Ra_C = \frac{\Delta \rho_C g D^3}{\kappa \eta_0}, \tag{6}$$

respectively, where α is thermal expansivity; ρ_0 is surface density with $C = T = 0$; g is gravitational acceleration; ΔT is the superadiabatic temperature difference across the mantle; D is the mantle thickness; κ is thermal diffusivity; η_0 is surface viscosity; and $\Delta \rho_C$ is the compositional density contrast between enriched and ambient mantle materials. Most of the benchmark problems considered here (all except problem 5) do not feature compositional heterogeneities. In those cases, $Ra_C = 0$, and the solution of equation 4 is not required. For problem 5, convection is isothermal with $Ra_T = 0$, and the solution of equation 3 is not required.

For variable viscosity cases, the formula used for the viscosity depends on the particular benchmark study. For problems 1, 3, and 4a, we have

$$\eta(T) = \exp\left[-\ln(\Delta\eta_T)T\right], \tag{7}$$

where $\Delta\eta_T$ is the maximum viscosity contrast in the system.

For problem 2, we have

$$\eta(T) = \exp\left[\frac{Q}{T+G} - \frac{Q}{0.5+G}\right], \tag{8}$$

with $Q = 225/\ln(\Delta\eta_T) - 0.25\ln(\Delta\eta_T)$ and $G = 15/\ln(\Delta\eta_T) - 0.5$.

In problem 4b, the rheology is non-Newtonian and is handled via an effective viscosity that contains both temperature- and strain rate-dependent terms. Specifically, the effective viscosity is

$$\eta(T, \dot{\epsilon}) = 2\left[\frac{1}{\eta_T(T)} + \frac{1}{\eta_{pla}(\dot{\epsilon})}\right]^{-1}, \tag{9}$$

with $\eta_T(T) = \exp\left[-\ln(\Delta\eta_T)T\right]$ and $\eta_{pla}(\dot{\epsilon}) = \eta^* + \tau_Y/(2\dot{\epsilon})$, where η^* is the minimum plastic viscosity and $\dot{\epsilon} = \left(\sqrt{\underline{\underline{\dot{\epsilon}}} : \underline{\underline{\dot{\epsilon}}}}\right)/2$ is the second invariant of the strain rate tensor.

Finally, for problem 6 the viscosity is given by

$$\eta(T) = \exp\left[\ln(\Delta\eta_T)(0.5 - T)\right]. \tag{10}$$

The diagnostic quantities used for benchmarking are the Root-Mean-Square (RMS) velocity, the mean temperature, and the surface and basal Nusselt numbers. The RMS velocity is given by

$$v_{RMS} = \left[\frac{1}{V}\int_V |\mathbf{v}|^2 dV\right]^{1/2}, \tag{11}$$

where V is the mantle volume. The mean temperature is

$$\bar{T} = \frac{1}{V}\int_V T dV. \tag{12}$$

The calculation of Nusselt numbers depends on geometry. For Cartesian geometry, the surface and basal Nusselt numbers are

$$Nu_{top} = Q_{top}/a \tag{13}$$

and

$$Nu_{bot} = Q_{bot}/a \tag{14}$$

respectively, where Q_{top} is the outward heat flux at the surface, Q_{bot} is the inward heat flux at the base and a is the aspect ratio. For spherical geometry, the surface and basal Nusselt numbers are (Zhong et al., 2008)

$$Nu_{top} = \frac{r_{top}(r_{top} - r_{bot})}{r_{bot}} Q_{top} \tag{15}$$

and

$$Nu_{bot} = \frac{r_{bot}(r_{top} - r_{bot})}{r_{top}} Q_{bot}, \tag{16}$$

with $r_{top} = 1.0$ and $r_{bot} = 0.55$ (i.e., a radial coordinate of zero corresponds to the center of the sphere).

3. COMSOL® Setup

In this study, we use COMSOL Multiphysics® 5.1 to model mantle convection (COMSOL Multiphysics®, 2015). This section provides details on setting up the software's modules to solve equations 1-4.

3.1. Geometry

For problems 1, 3, 4, and 5, rectangles are used to specify the problem geometry. For these problems, a unit aspect ratio is used, except for problem 5, which uses an aspect ratio of 0.9142. For problem 2, a rectangular block is used for the geometry. In this problem, block dimensions of $1.0079 \times 0.6283 \times 1$ (isoviscous case) and $1 \times 1 \times 1$ (variable viscosity case) are used. For problem 6, spheres are used to define the problem geometry. Specifically, the spherical shell of the mantle is created by taking a difference between an outer and inner sphere, with radii of 1.00 and 0.55, respectively. In COMSOL®, spatial discretization of the model geometry is performed using finite elements. Specific element details are given below.

3.2. Laminar Flow Physics Module

The laminar flow physics module is used to solve equations 1 and 2 for all problems. The incompressible flow option is used in all cases. Although mantle convection occurs in the infinite Prandtl number regime, this module only allows a finite value to be specified. For all problems, a Prandtl number of 10^{20} is used. The buoyancy terms of equation 2 are implemented by adding a volume force along the direction of gravity in the module. Free-slip conditions are applied at all domain boundaries except in problem 5, where no-slip (i.e., rigid) conditions are applied at the top and bottom boundaries. Further, a pressure point constraint is applied on one boundary point in all domains to eliminate non-uniqueness issues. All problems utilize first-order elements for pressure. For velocity, all problems use second-order elements except problems 2 and 5, which use first-order elements (more details below).

3.3. Heat Transfer in Fluids Physics Module

This module solves equation 3 for all problems except problem 5, which is isothermal. All applicable problems utilize second-order elements, except problem 2, in which first-order elements are used to reduce computational expense. Nonetheless, COMSOL® produces accurate benchmark results for this problem (see section 4.2). Constant temperature boundary conditions are applied to the surface and base for all problems. For all Cartesian cases, insulation conditions are applied along sidewalls.

3.4. Transport of Diluted Species Module

This module is only used in problem 5 to apply a level set method for solving equation 4 (described in detail in section 4.5). To minimize spurious oscillations and overdiffusion due to steep gradients, first-order finite elements are used with a diffusion coefficient of 10^{-9} for stabilization. Zero flux conditions are applied at all boundaries.

3.5. Multiphysics Module

The multiphysics module enables feedback between physics modules. In mathematical terms, this allows coupling of the governing equations 1-4. For all problems, flow coupling is added to the multiphysics module in order to feed the velocity field obtained from the laminar flow module into either the heat transfer in fluids module (problems 1-4 and 6) or the transport of diluted species module (problem 5).

For all problems except 5, temperature coupling is added to the multiphysics module. This gives the laminar flow module access to the temperature field generated by the heat transfer in fluids module, enabling temperature-dependent buoyancy and viscosity.

For problem 5, the concentration variable representing mantle composition must be manually inserted into the volume force term of the laminar flow module. This is because a multiphysics option for the concentration variable analogous to temperature coupling is not available in the GUI.

3.6. Mesh Selection

In problems 1, 3, and 4, a mesh comprised of 12 000 quadrilateral elements is used with boundary layer refinement near the top and bottom boundaries (shown in figure 1a). For problems 2a and b, meshes composed of 37 276 and 94 124 finite elements (mainly tetrahedral) are used, shown in figure 1b. Boundary layer refinement is used at the surface and base of both domains.

For problem 5, adaptive mesh refinement is used with an initial mesh composed of 10 520 triangular elements (shown in figure 1c). We find that the default error estimator function used to refine the mesh did not produce reasonable results. However, utilizing a user-defined error estimator function of the L_2 norm of ∇c, where c is the concentration variable from the transport of diluted species module, offers significant improvement. The time evolution of the mesh using this error estimator is shown in section 4.5.

In problem 6, 142 776 tetrahedral elements are used (shown in figure 1d). In this case, boundary layer refinement is not used. Calculations were attempted using boundary layer refinement, but they were not able to obtain the desired tetrahedral thermal planform for this benchmark problem.

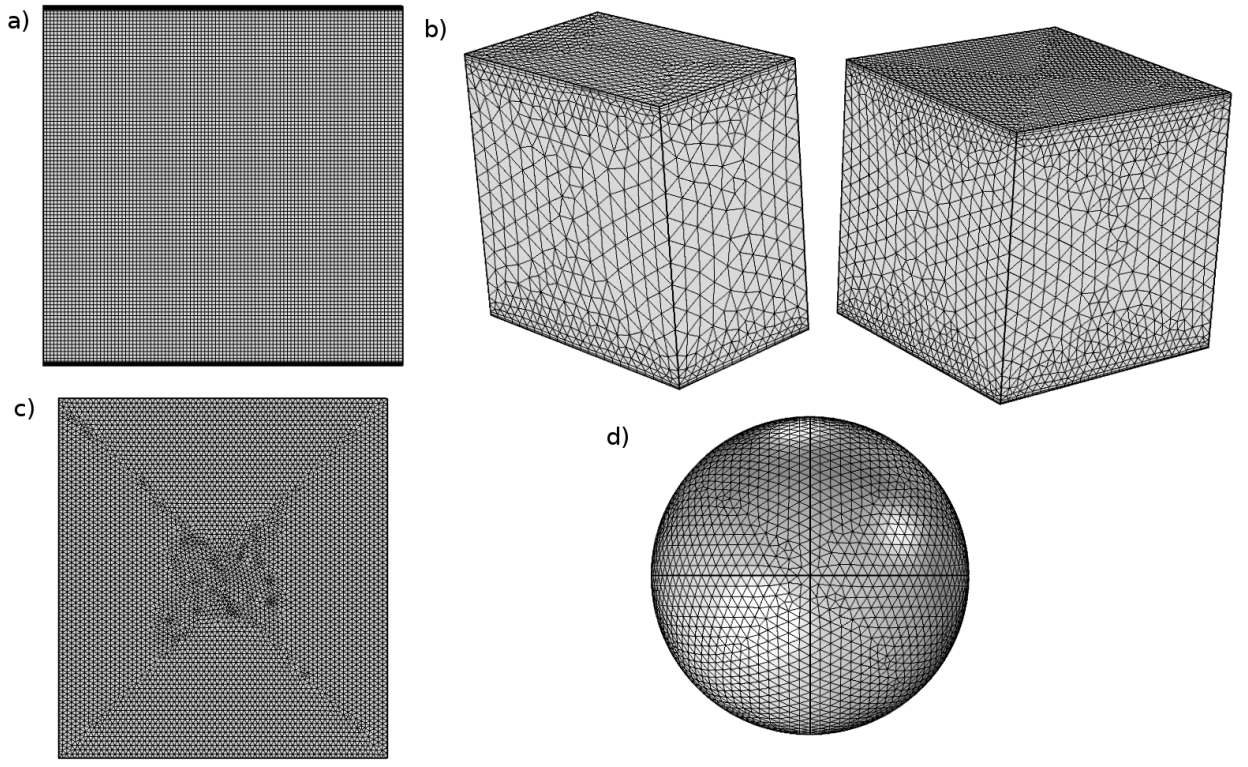

Figure 1: Snapshots of the finite element meshes used in a) problems 1, 3 and 4; b) problem 2; c) problem 5; and d) problem 6. For part c, the initial mesh is shown (see figure 4 for time evolution of the mesh due to adaptive mesh refinement).

3.7. Study Options

In COMSOL®, the choice of study indicates how model time is interpreted by the software. Specifically, there are time-dependent and stationary studies depending upon whether the calculation at hand requires a time-accurate or steady-state solution.

Problems 1-4 make use of the stationary study option in order to reach steady state in an efficient manner. On the other hand, problem 5 uses the time-dependent study option. For problem 6, there are multiple steady-state solutions possible, and the details of temporal evolution can affect the particular steady solution obtained. Accordingly, the time-dependent study option is used for problem 6.

4. Results

A summary of benchmark values produced by COMSOL® and the corresponding values from previous studies are shown in table 2. Specifically, the RMS velocity (v_{RMS}), surface Nusselt number (Nu_{top}), basal Nusselt number (Nu_{bot}) and mean temperature ($\bar{T}$) are shown, where applicable.

Table 2
Summary of benchmark values. For each problem, results are presented in two rows. The upper rows contain results produced by COMSOL® while the lower rows contain previously reported values from the defining benchmark studies. For problem 3, the precise data values are not available (Moresi and Solomatov (1995) present their results in graphical format). For problem 4, the ranges of values from Tosi et al. (2015) are given. In problem 5, the peak RMS velocity is given.

Problem	v_{RMS}	Nu_{top}	Nu_{Bot}	$\bar{T}$
1a	834.00298	21.973177		
	833.98977	21.972465		
1b	479.3267	10.0416		
	480.4334	10.0660		
2a	40.878	3.5502		
	40.999	3.5374		
2b	34.95	3.0260		
	35.13	3.0393		
3	88.5735	1.5571		
4a	249.5700	3.4216	3.4372	0.7757
	248.9252–252.0906	3.4091–3.5889	3.313–3.4259	0.7758–0.7768
4b	140.6447	8.54884	8.57334	0.6034
	140.1871–143.8518	8.5115–8.74753	8.3990–8.6489	0.6027–0.6071
5	0.002851			
	0.003091			
6a	33.34	3.5157	3.5153	0.2578
	32.66	3.5126	3.4919	0.2171
6b	26.95	3.1879	3.2433	0.2342
	27.36	3.2674	3.2491	0.2360
6c	25.42	3.0876	3.1552	0.2412
	25.85	3.1724	3.1548	0.2432
6d	22.62	2.8404	2.9265	0.2625
	23.11	2.9354	2.9205	0.2653
6e	22.76	2.1577	2.2480	0.2892
	22.90	2.5468	2.5352	0.3124

4.1. Problem 1

Problem 1a features 2D Cartesian isoviscous flow with $Ra_T = 10^6$ (case 1c from Blankenbach et al. (1989)). A snapshot of the steady-state temperature field is given in figure 2a. Due to thin thermal boundary layers, mesh refinement was essential for accurate modeling of surface and basal heat fluxes. The RMS velocity and Nusselt number produced in COMSOL® match the best values within 0.002% and 0.004%, respectively.

For problem 1b, temperature-dependent viscosity given by equation 7 is introduced with $\Delta\eta_T = 10^3$ and $Ra_T = 10^4$ at the surface (case 2a from Blankenbach et al. (1989)). This causes the cold lid of the system to stagnate and thicken, as shown in figure 2b. The resulting RMS velocity and surface Nusselt number both agree with Blankenbach et al. (1989) within 0.3%. To help the convergence of COMSOL®'s stationary solver, this calculation was performed using a sequence of steady-state calculations with increasing $\Delta\eta_T$ values. Specifically, $\Delta\eta_T$ was increased from 1 to 10^3 in half-decade increments.

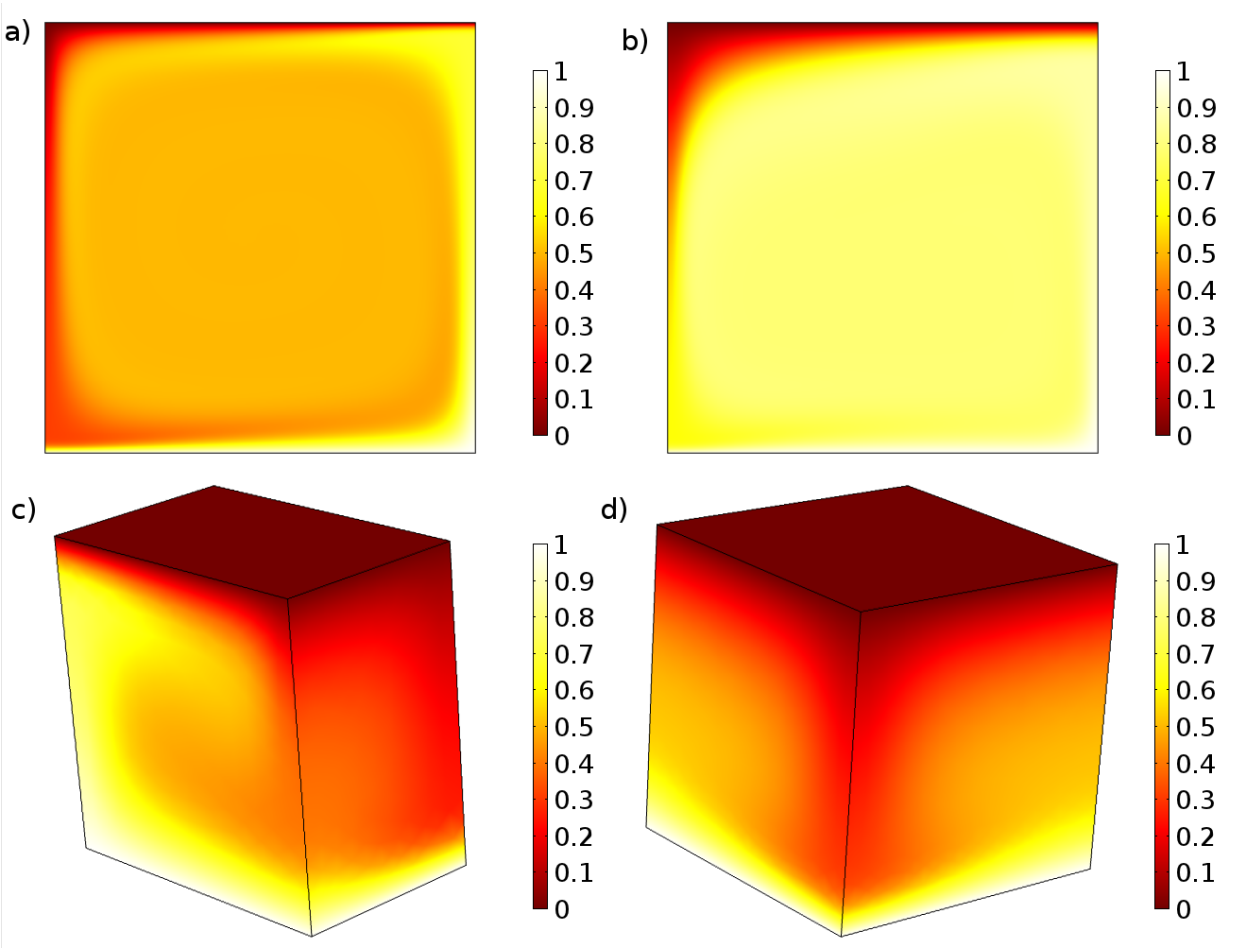

Figure 2: Steady-state temperature snapshots for a) problem 1a, b) problem 1b, c) problem 2a and d) problem 2b. For 3D plots, temperature is shown for the domain boundaries.

4.2. Problem 2

Problem 2a consists of 3D Cartesian isoviscous flow with $Ra_T = 3 \times 10^4$ (case 1a from Busse et al. (1994)). The steady-state temperature field is shown in figure 2c. Due to the relatively low value of Ra_T, thermal diffusion leads to thick thermal boundary layers. The RMS velocity and Nusselt numbers produced with COMSOL® agree with the results of Busse et al. (1994) within 0.3% and 0.4%, respectively.

In problem 2b, viscosity varies with temperature according to equation 8 with $\Delta\eta_T = 20$ and $Ra_T = 2 \times 10^4$ (case 2 from Busse et al. (1994)). The steady-state temperature field, presented in figure 2d, exhibits a thicker lid due to the temperature dependence of viscosity. For this case, the RMS velocity and surface Nusselt number agree with the values given in Busse et al. (1994) within 0.6% and 0.5%, respectively.

4.3. Problem 3

For problem 3, an extremely temperature-dependent viscosity is tested within a 2D Cartesian geometry. Specifically, the viscosity is given by equation 7 with $\Delta\eta_T = 10^{10}$ and a corresponding surface Ra_T value of 10^{-3} (the basal Rayleigh number is 10^7). A snapshot of the steady-state temperature solution is shown in figure 3a. Due to viscous decoupling, the interior flows nearly independently from the surface leading to an immobile lid. This is known as stagnant-lid convection. Similar to problem 1b, a sequence of steady-state calculations featuring increasing $\Delta\eta_T$ values was performed. Specifically, $\Delta\eta_T$ was varied between 10 and 10^{10} using half-decade intervals. Because Moresi and Solomatov (1995) define the problem using a basal Rayleigh number, the surface value used in equation 2 must be updated as $Ra_T = 10^7/\Delta\eta_T$ for each intermediate steady-state calculation. The surface Nusselt number obtained with COMSOL® is 1.5571, consistent with the data of figure 5 in Moresi and Solomatov (1995).

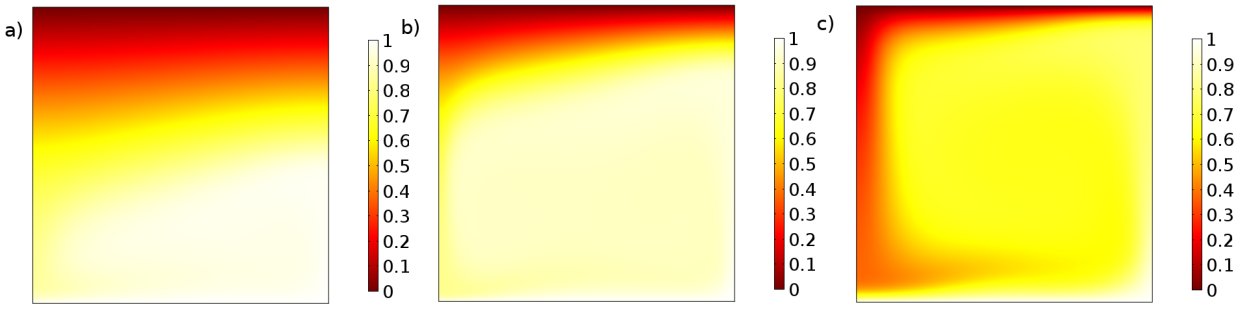

Figure 3: Steady-state temperature snapshots for a) problem 3, b) problem 4a, and c) problem 4b.

4.4. Problem 4

For problem 4a, a temperature-dependent rheology is presumed (equation 7) with $\Delta\eta_T = 10^5$ and $Ra_T = 10^2$ (case 1 from Tosi et al. (2015)). The temperature dependence is sufficiently strong to form stagnant-lid convection, as shown in figure 3b. The resulting steady-state RMS velocity and surface Nusselt numbers fall within the range produced by the codes participating in Tosi et al. (2015). The basal Nusselt number and mean temperature fall just outside the published ranges by 0.33% and 0.013%, respectively.

Problem 4b features a viscoplastic rheology where viscosity varies with both temperature and strain rate (equation 9, equivalent to case 2 of Tosi et al. (2015)). For deviatoric stresses below the yield stress, temperature dependence dominates, and mantle material deforms viscously. When deviatoric stresses exceed the yield stress, material deforms plastically. Problem 4b features a yield stress value of $\tau_Y = 1$ with a minimum plastic viscosity of $\eta^* = 10^{-3}$. As before, $\Delta\eta_T = 10^5$ and $Ra_T = 10^2$. Due to plastic yielding near the surface, the steady-state flow exhibits strong convective coupling between the surface and the interior (mobile-lid convection). Similar to problems 1b and 3, a sequence of steady-state calculations was performed in COMSOL® in order to improve the convergence of the stationary solver. In particular, the initial calculation was made using $\tau_Y = 10$ and reduced in unit intervals. The RMS velocity, Nusselt numbers, and mean temperature values all lie within the published ranges.

4.5. Problem 5

Problem 5 consists of a time-dependent, isoviscous Rayleigh–Taylor instability. In this case, a buoyant layer ($Ra_T = 0$ and $Ra_C = -1$) near the model base is given a sinusoidal perturbation with an amplitude of 0.1, leading to gravitational instability. For this problem, equation 4 should be solved. However, it is challenging to do so numerically because of the absence of diffusion. An established numerical method for the problem is the level set method. Unfortunately, COMSOL® version 5.1 does not have this feature for the basic package. However, we can emulate the level set method using the transport of diluted species module that solves an advection-diffusion equation for concentration. By specifying a small diffusion coefficient (10^{-9}) to improve numerical stability, we can use the

concentration field as an approximate level set. To further reduce numerical errors in the presence of sharp gradients, we employ adaptive mesh refinement in COMSOL®'s solver options. One aspect of a true level set formulation that is lacking in this approach is level set reinitialization that preserves smoothness in the level set. However, this problem is simulated for a relatively small amount of advection (only two substantial buoyant diapirs form), and this reduces the need for reinitialization. We choose a concentration value of 0.5 to represent the interface between materials. The initial finite element mesh and concentration field are shown in figure 4a and e. Concentration values above and below 0.5 correspond to C values of 0 and 1 in equation 4, respectively. Figure 4 parts b-d and f-h show snapshots of the mesh and concentration fields at nondimensional times of 500, 1000, and 1500. The 0.5 contour of the concentration field is similar to the "best" result (model PvK 80×80) from van Keken et al. (1997). The observed peak RMS velocity value undershoots the best value by 7.8%, possibly due to the artificial diffusion added to stabilize the advection of the concentration field. In future work, the level set solver in COMSOL®'s multiphase flow package should be tested. Using a true level set approach is expected to improve the accuracy of the peak value.

4.6. Problem 6

Problems 6a–e feature steady-state mantle convection in a spherical geometry (equivalent to cases A1–A5 from Zhong et al. (2008)). For this problem, $Ra_T = 7 \times 10^3$, and viscosity is determined using equation 10 with $\Delta\eta_T$ set to a) 1, b) 10, c) 20, d)100, and e) 1000. Snapshots of the steady-state temperature fields for these cases are shown in figure 5. The steady-state values for RMS velocity, surface and basal Nusselt numbers, and mean temperature are presented in table 2. For the calculation of the RMS velocities, we have removed any contributions due to passive rotation (uniform rotation that depends on the particular selection of coordinate axes and does not impact stresses). We find that the steady-state thermal planform is sensitive to the initial condition used. In Zhong et al. (2008), an analytic initial condition is proposed that leads to tetrahedral planforms in their study. However, in COMSOL® we find that the analytic initial condition only produces tetrahedral planforms in problems 6a and b. In order to obtain tetrahedral planforms in problems 6c and d, we used the final state of the next lowest viscosity contrast as the initial condition.

Although we obtain a tetrahedral planform for problem 6a, it is noticeably different in character compared to the planforms of problems 6b–d and that of Zhong et al. (2008). Our model appears to have evolved into an alternate tetrahedral configuration. Due to this variation in planform, the mean temperature differs from the result of Zhong et al. (2008) by 18.7%. However, the RMS velocity, surface Nusselt number and basal Nusselt number agree within 2.1%, 0.088%, and 0.67%, respectively.

The planforms obtained for problems 6b–d match the results of Zhong et al. (2008) closely. For these cases, the RMS velocity, surface Nusselt number, basal Nusselt number, and mean temperature agree with those reported in Zhong et al. (2008) within 2.2%, 3.2%, 0.2%, and 1.1%, respectively.

For problem 6e, we were unable to produce a tetrahedral planform, even using the final state of problem 6d as the initial condition. We also tried using generalized alpha time-stepping in place of the COMSOL® default backward differentiation formula (BDF) method to no avail. In all of our attempts, we obtain a bimodal thermal planform. Despite this, the RMS velocity still agrees with the tetrahedral solution obtained by Zhong et al. (2008) within 0.7%. However, due to the difference in thermal planform the values of Nu_{top}, Nu_{bot}, and $\bar{T}$ differ by 15.3%, 11.3%, and 7.4%, respectively.

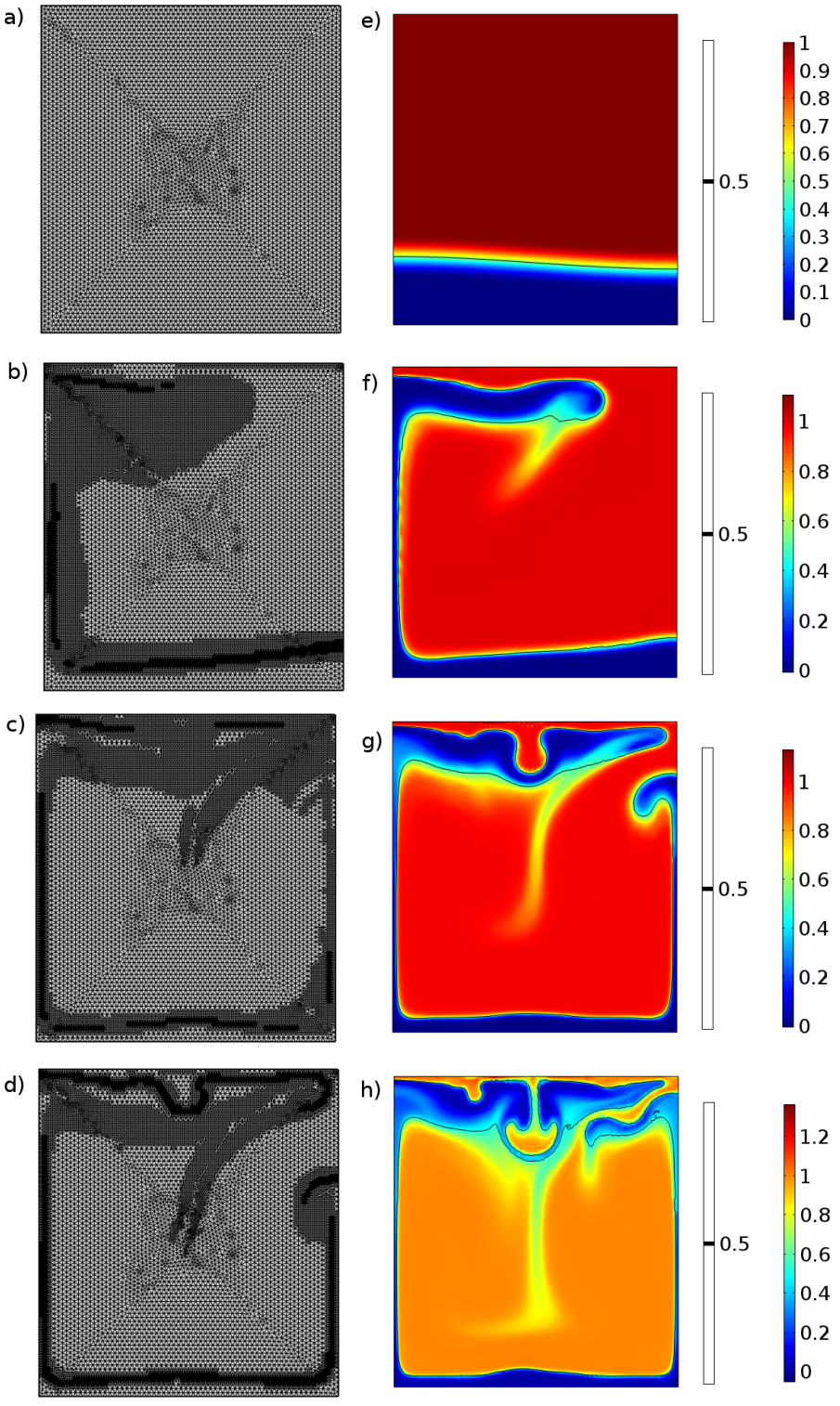

Figure 4: Snapshots for the time-dependent Rayleigh–Taylor instability of problem 5. Parts a–d show the finite element mesh corresponding to nondimensional times of 0, 500, 1000, and 1500. Parts e–h show the numerical concentration field at the same nondimensional times. The 0.5 contour of the numerical concentration field is also shown, representing the interface between enriched and ambient materials.

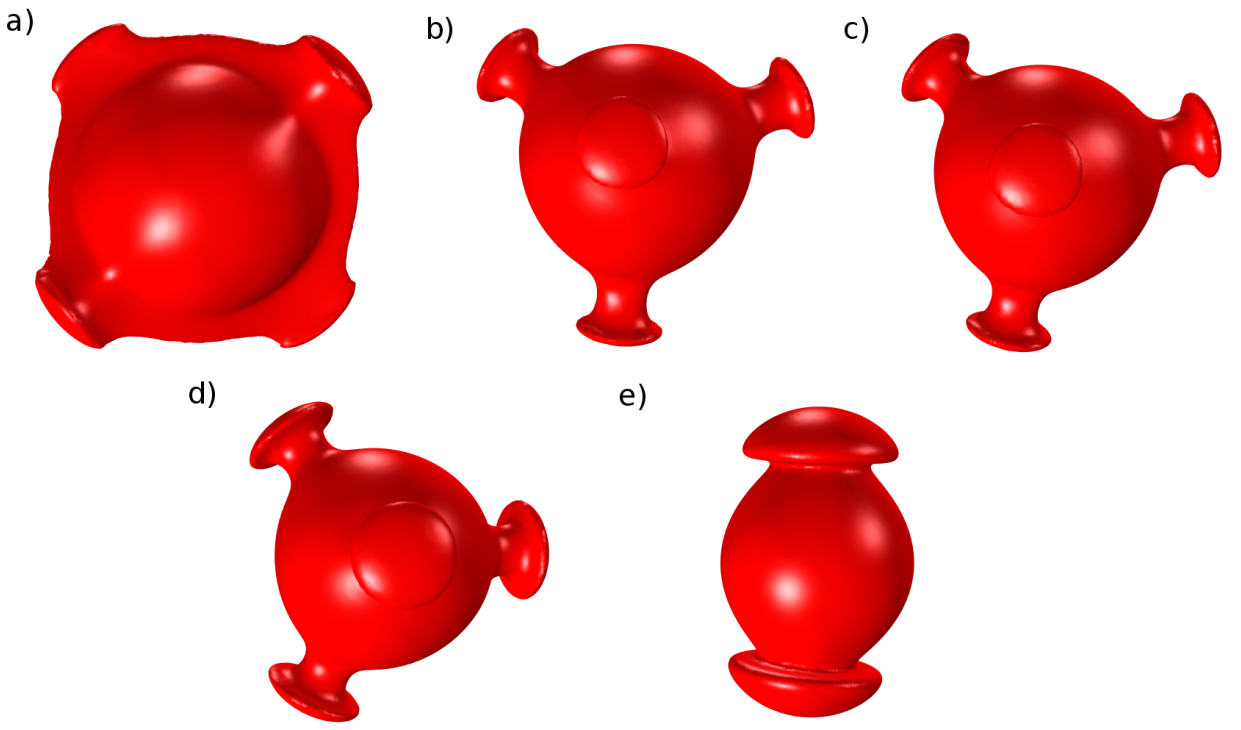

Figure 5: Steady-state snapshots of temperature for problem 6. Isosurfaces corresponding to T =0.6 are shown. The z-axis is out of the page for a, d, and e and into the page for b and c.

5. Discussion and Conclusions

For the diagnostic quantities analyzed, our results for problems 1, 2, and 4 agree with the reported values within much less than 1%. Accordingly, COMSOL® can accurately model isoviscous, temperature-dependent viscosity and viscoplastic flows. Additionally, our findings from problem 3 are consistent with the plots in Moresi and Solomatov (1995), confirming COMSOL®'s ability to function with more extreme viscosity contrasts. For problem 5, the predicted configuration of the compositional interface closely matches the results from (van Keken et al., 1997). However, the peak RMS velocity is lower than the reported values. This is likely due to artificial diffusion added in the solution process and can potentially be minimized by the use of COMSOL®'s level set or phase field methods[1].

For problems 6b–d, we obtain good agreement with the results of Zhong et al. (2008). However, we find that achieving a particular steady-state solution difficult in general. For part a, we achieve a steady-state solution that is tetrahedral in nature yet differs in character from the steady-state found by Zhong et al. (2008). For part e, we were unable to achieve a tetrahedral solution. Instead, our solutions evolve to a bimodal state. We speculate that perhaps the tetrahedral state is unstable to perturbations at larger viscosity contrasts.

We have tested a range of mantle dynamics features. However, there are still several other facets that should

[1]This requires access to the multiphase flow software package.

be tested in the future. For example, compressible convection is an option within the laminar flow physics module (following the work of Lee (2014)). Thermochemical convection should also be tested using the level set and phase field methods. We tested a viscoplastic rheology in problem 4, which is one avenue for tectonic plate modeling in mantle convection. However, another candidate for testing is the force-balanced plate model (e.g., Gable et al., 1991; Shiels and Butler, 2015). Also, 2D geometries with curvature, such as cylindrical geometry, should be tested. In addition to mantle convection, it is of future interest to assess the accuracy of COMSOL® for other types of geodynamic models, such as lithosphere dynamics and core convection.

6. Acknowledgements

This article was supported by the Natural Sciences and Engineering Research Council of Canada (RGPIN 228090-2013).

7. Data Availability

The dataset supporting this article may be found at `http://doi.org/10.5281/zenodo.3728213`, hosted by Zenodo (Trim et al., 2020). This dataset is comprised of input files for each problem, containing initial and final output data. The input files may be used as templates for future studies.

8. Code Availability

COMSOL® 5.1 input script files are also found at `http://doi.org/10.5281/zenodo.3728213`, hosted by Zenodo (Trim et al., 2020).

References

Azad, V.J., Li, C., Verba, C., Ideker, J.H., Isgor, O.B., 2016. A COMSOL–GEMS interface for modeling coupled reactive-transport geochemical processes. Computers & Geosciences 92, 79–89.

Bird, M., Butler, S.L., Hawkes, C., Kotzer, T., 2014. Numerical modeling of fluid and electrical currents through geometries based on synchrotron X-ray tomographic images of reservoir rocks using Avizo and COMSOL. Computers & Geosciences 73, 6–16.

Blankenbach, B., Busse, F., Christensen, U., Cserepes, L., Gunkel, D., Hansen, U., Harder, H., Jarvis, G., Koch, M., Marquart, G., et al., 1989. A benchmark comparison for mantle convection codes. Geophysical Journal International 98, 23–38.

Buffett, B.A., 2002. Estimates of heat flow in the deep mantle based on the power requirements for the geodynamo. Geophysical Research Letters 29, 7–1.

Busse, F., Christensen, U., Clever, R., Cserepes, L., Gable, C., Giannandrea, E., Guillou, L., Houseman, G., Nataf, H., Ogawa, M., et al., 1994. 3D convection at infinite Prandtl number in Cartesian geometry—A benchmark comparison. Geophysical & Astrophysical Fluid Dynamics 75, 39–59.

Butler, S.L., Sinha, G., 2012. Forward modeling of applied geophysics methods using Comsol and comparison with analytical and laboratory analog models. Computers & Geosciences 42, 168–176.

Butler, S.L., Zhang, Z., 2016. Forward modeling of geophysical electromagnetic methods using Comsol. Computers & Geosciences 87, 1–10.

COMSOL Multiphysics®, 2015. COMSOL Multiphysics® version 5.1: user's guide. Burlington .

Gable, C.W., O'Connell, R.J., Travis, B.J., 1991. Convection in three dimensions with surface plates: Generation of toroidal flow. Journal of Geophysical Research: Solid Earth 96, 8391–8405.

Gubbins, D., Willis, A.P., Sreenivasan, B., 2007. Correlation of Earth's magnetic field with lower mantle thermal and seismic structure. Physics of the Earth and Planetary Interiors 162, 256–260.

Halloran, L.J., Brunner, P., Hunkeler, D., 2019. COMPEST, a PEST-COMSOL interface for inverse multiphysics modelling: Development and application to isotopic fractionation of groundwater contaminants. Computers & Geosciences 126, 107–119.

Herein, M., Galsa, A., 2011. The effect of different geometries on the thermal mantle convection, in: 6th Congress of the Balkan Geophysical Society, European Association of Geoscientists & Engineers. pp. cp–262.

Humayun, M., Qin, L., Norman, M.D., 2004. Geochemical evidence for excess iron in the mantle beneath Hawaii. Science 306, 91–94.

Ishii, M., Tromp, J., 2004. Constraining large-scale mantle heterogeneity using mantle and inner-core sensitive normal modes. Physics of the Earth and Planetary Interiors 146, 113–124.

Labrosse, S., Hernlund, J., Coltice, N., 2007. A crystallizing dense magma ocean at the base of the Earth's mantle. Nature 450, 866–869.

Lee, C., 2014. Effects of radiogenic heat production and mantle compressibility on the behaviors of Venus' and Earth's mantle and lithosphere. Geosciences Journal 18, 13–30.

Lee, C., Wada, I., 2017. Clustering of arc volcanoes caused by temperature perturbations in the back-arc mantle. Nature communications 8, 1–9.

Li, Y., Smith, R.S., 2015. Forward modeling of radio imaging (RIM) data with the Comsol RF module. Computers & Geosciences 85, 60–67.

McNamara, A.K., Zhong, S., 2005. Thermochemical structures beneath Africa and the Pacific Ocean. Nature 437, 1136–1139.

Moresi, L.N., Solomatov, V., 1995. Numerical investigation of 2D convection with extremely large viscosity variations. Physics of Fluids 7, 2154–2162.

Nardi, A., Idiart, A., Trinchero, P., de Vries, L.M., Molinero, J., 2014. Interface COMSOL-PHREEQC (iCP), an efficient numerical framework for the solution of coupled multiphysics and geochemistry. Computers & Geosciences 69, 10–21.

Pirnia, P., Duhaime, F., Ethier, Y., Dubé, J.S., 2019. ICY: An interface between COMSOL multiphysics and discrete element code YADE for the modelling of porous media. Computers & Geosciences 123, 38–46.

Shahraki, M., Schmeling, H., 2012. Plume-induced geoid anomalies from 2d axi-symmetric temperature-and pressure-dependent mantle convection models. Journal of Geodynamics 59, 193–206.

Shiels, C., Butler, S., 2015. Couette and Poiseuille flows in a low viscosity asthenosphere: Effects of internal heating rate, Rayleigh number, and plate representation. Physics of the Earth and Planetary Interiors 246, 31–40.

Sinha, G., Butler, S., 2009. The combined effects of continents and the 660 km-depth endothermic phase boundary on the thermal regime in the mantle. Physics of the Earth and Planetary Interiors 173, 354–364.

Tosi, N., Stein, C., Noack, L., Hüttig, C., Maierova, P., Samuel, H., Davies, D.R., Wilson, C.R., Kramer, S.C., Thieulot, C., et al., 2015. A community benchmark for viscoplastic thermal convection in a 2-D square box. Geochemistry, Geophysics, Geosystems 16, 2175–2196.

Trim, S., Butler, S., Spiteri, R., 2020. Dataset for Article Titled Benchmarking Multiphysics Software. URL: https://doi.org/10.5281/zenodo.3728213, doi:10.5281/zenodo.3728213.

Trim, S., Heron, P., Stein, C., Lowman, J., 2014. The feedback between surface mobility and mantle compositional heterogeneity: Implications for

the Earth and other terrestrial planets. Earth and Planetary Science Letters 405, 1–14.

Trim, S.J., Lowman, J.P., 2016. Interaction between the supercontinent cycle and the evolution of intrinsically dense provinces in the deep mantle. Journal of Geophysical Research: Solid Earth 121, 8941–8969.

Turcotte, D.L., Schubert, G., 2002. Geodynamics. Cambridge university press.

van Keken, P., King, S., Schmeling, H., Christensen, U., Neumeister, D., Doin, M.P., 1997. A comparison of methods for the modeling of thermochemical convection. Journal of Geophysical Research: Solid Earth 102, 22477–22495.

Zhong, S., McNamara, A., Tan, E., Moresi, L., Gurnis, M., 2008. A benchmark study on mantle convection in a 3-D spherical shell using CitcomS. Geochemistry, Geophysics, Geosystems 9.